

A NEW CHANNEL FOR DETECTING DARK MATTER SUBSTRUCTURE IN GALAXIES: GRAVITATIONAL LENS TIME DELAYS

CHARLES R. KEETON¹ AND LEONIDAS A. MOUSTAKAS²

¹ Department of Physics & Astronomy, Rutgers University, 136 Frelinghuysen Road, Piscataway, NJ 08854, USA

² Jet Propulsion Laboratory, California Institute of Technology, 4800 Oak Grove Drive, MS 169-327, Pasadena, CA 91109, USA

To appear in ApJ

ABSTRACT

We show that dark matter substructure in galaxy-scale halos perturbs the time delays between images in strong gravitational lens systems. The variance of the effect depends on the subhalo mass function, scaling as the product of the substructure mass fraction and a characteristic mass of subhalos (namely $\langle m^2 \rangle / \langle m \rangle$). Time delay perturbations therefore complement gravitational lens flux ratio anomalies and astrometric perturbations by measuring a different moment of the subhalo mass function. Unlike flux ratio anomalies, “time delay millilensing” is unaffected by dust extinction or stellar microlensing in the lens galaxy. Furthermore, we show that time delay *ratios* are immune to the radial profile degeneracy that usually plagues lens modeling. We lay out a mathematical theory of time delay perturbations and find it to be tractable and attractive. We predict that in “cusp” lenses with close triplets of images, substructure may change the arrival-time order of the images (compared with smooth models). We discuss the possibility that this effect has already been observed in RX J1131–1231.

Subject headings: dark matter — gravitational lensing — time

1. INTRODUCTION

The cold dark matter (CDM) paradigm predicts that 5%–10% of each galaxy’s mass is bound up in subhalos left over from the hierarchical formation process. In the Local Group, the predicted number of dark matter subhalos significantly exceeds the observed number of dwarf galaxy satellites (e.g., Moore et al. 1999; Klypin et al. 1999; Strigari et al. 2007a; Koposov et al. 2008). The abundance of substructure depends on competition between accretion of new subhalos from the environment and destruction of old subhalos by tidal forces (e.g., Taylor & Babul 2001, 2004; Benson et al. 2002; Zentner & Bullock 2003; Koushiappas et al. 2004; Oguri & Lee 2004; van den Bosch et al. 2005; Zentner et al. 2005). Also, the number of subhalos that “light up” and become visible as satellite galaxies depends on whether subhalos are able to retain their gas against photoevaporation, and on the efficiency of galaxy formation in low-mass systems (e.g., Bullock et al. 2000; Somerville 2002; Kravtsov et al. 2004; Koposov et al. 2009; Macciò et al. 2009). Measuring the amount of substructure in galaxy halos, and how it varies with galaxy mass, environment, and redshift, therefore provides unique access to the astrophysics of galaxy formation on small scales.

We still know very little about the physical properties of the dark matter particle, but a number of specific models have been proposed: dark matter could be sterile neutrinos, or supersymmetric particles, or a manifestation of extra dimensions, or even a product from the decay of any of these particles (e.g., Dodelson & Widrow 1994; Cheng et al. 2002; Feng 2005; Strigari et al. 2007b). All of those possibilities are compatible with observations that probe the universe on large scales. However, they make some different predictions about the amount of dark matter substructure; for example, any type of “warm” dark matter can lead to a suppression of power on small scales (e.g., Colín et al. 2000; Davé et al. 2001; Zentner & Bullock 2003). Studying galaxy substructure provides the opportunity to test such models and obtain

important astrophysical evidence about the fundamental nature of dark matter.

Strong gravitational lensing is a simple geometric phenomenon that gives us a valuable tool for studying mass in distant galaxies, including substructure. Lensing effects are succinctly encoded in the properties of the time delay surface. Consider light emitted by a background source at angular position u from the center of a foreground lens with (projected) potential ϕ .¹ If the light reaches us from the angular image position x , the excess travel time relative to a hypothetical light ray that travels directly from the source with no deflection is

$$\tau(x) = t_0 \left[\frac{1}{2} |x - u|^2 - \phi(x) \right], \quad t_0 = \frac{1 + z_l}{c} \frac{D_l D_s}{D_{ls}}. \quad (1)$$

By Fermat’s principle, images form at stationary points of the time delay surface, i.e., positions x such that $\nabla \tau(x) = 0$. (This directly yields the lens equation, usually written as $u = x - \nabla \phi$.) The magnifications of the images are determined by second derivatives of τ (and hence depend on second derivatives of the lens potential ϕ). What is usually measured is the differential time delay between two images, $\Delta t_{ij} = \tau(x_j) - \tau(x_i)$. (See the review of strong lensing by Kochanek et al. 2004 for more details.)

Strong lensing provides the only way to detect substructure directly (i.e., by virtue of its gravity) in galaxies outside the Local Group. Small mass clumps in the lens galaxy can strongly perturb lensed images. The spatial perturbations are determined by first derivatives of the lens potential: they have angular scales of milli-arcseconds for “millilensing” by dark matter subhalos (e.g., Mao & Schneider 1998; Metcalf & Madau 2001; Chiba 2002; Dalal & Kochanek 2002; Metcalf et al. 2004; Chen et al. 2007), or micro-arcseconds for “microlensing” by stars

¹ The lens potential ϕ is a scaled version of the two-dimensional gravitational potential. Specifically, it satisfies the Poisson equation $\nabla^2 \phi = 2\Sigma / \Sigma_{\text{crit}}$ where Σ is the surface mass density of the lens, and Σ_{crit} is the critical surface density for lensing.

TABLE 1
REFERENCE IMAGES: “FOLD” LENS

Image	New Label	x (")	y (")	μ	Δt (days)
C	M1	0.343	1.360	3.85	$\equiv 0$
A1	M2	-0.948	-0.697	13.66	10.77
A2	S1	-1.098	-0.206	-12.50	10.93
B	S2	0.700	-0.652	-3.02	17.82

NOTE. — Reference smooth images for our sample fold lens similar to PG 1115+080. All coordinates are given in arcseconds with respect to the center of the lens galaxy at (0,0). The time delays are given with respect to the leading image. The sign of the magnification (μ) represents the image parity. Col. 1 gives the traditional image names for PG 1115+080, while Col. 2 gives our new labels: “M” and “S” indicate (respectively) an image at a local minimum or saddlepoint of the time delay surface, while “1” and “2” indicate (respectively) the leading and trailing image of each type.

in the lens galaxy (e.g., Witt et al. 1995; Wyithe et al. 2000; Schechter & Wambsganss 2002; Kochanek et al. 2007; Congdon et al. 2007). Since lensing magnifications depend on second derivatives of the lens potential, they are even more sensitive to substructure: magnification perturbations can be of order unity and are therefore very apparent, especially in 4-image lenses (e.g., Metcalf & Zhao 2002; Keeton, Gaudi & Petters 2003, 2005).

At optical and X-ray wavelengths quasar emission regions are small enough that lens flux ratios are sensitive to both dark matter subhalos and stars (e.g., Kochanek et al. 2007; Keeton et al. 2006; Blackburne et al. 2006; Pooley et al. 2007); this makes it difficult to isolate millilensing and study dark matter substructure. By contrast, at radio wavelengths the quasar source is thought to be large enough to smooth over the effects of stars and be insensitive to microlensing (but see Koopmans & de Bruyn 2000). The flux ratios of radio lenses (especially 4-image, or quad, lenses) have therefore been the tool of choice for studying millilensing. The amount of substructure needed to explain radio lens flux ratios is broadly consistent with CDM predictions (Dalal & Kochanek 2002). The greatest limitation of this method is the small number of radio quads known currently (e.g., Browne et al. 2003).

In this paper we show that lens *time delays* provide an exciting new way to probe dark matter substructure, with several distinct advantages. As we shall see, time delays are not affected by microlensing, so we can use optical as well as radio data to probe dark matter substructure; this is important because there will be thousands of lenses discovered in new optical surveys (e.g., Fassnacht et al. 2004; Kuhlen et al. 2004; Marshall et al. 2005; Kochanek et al. 2006), complementing new samples of radio lenses (e.g., Koopmans et al. 2004). Time delays are sensitive to the mass function of dark matter subhalos in a way that flux ratios are not; so they offer a good opportunity to probe the masses of subhalos in distant galaxies. By all indications the theory of time delay millilensing is very tractable; having a formal theory will provide a rigorous foundation for substructure studies, and may even allow us to do some of the statistics analytically. Appropriate time delay measurements are feasible now, and truly revolutionary datasets will become available in the foreseeable future.

For the purpose of concreteness, we assume a cosmology with $\Omega_M = 0.3$, $\Omega_\Lambda = 0.7$, and $H_0 = 70 \text{ km s}^{-1} \text{ Mpc}^{-1}$, and we adopt specific values for the lens and source redshifts (motivated by particular lens systems, as discussed below). Modifying the cosmology or the lens and source redshifts would

TABLE 2
REFERENCE IMAGES: “CUSP” LENS

Image	New Label	x (")	y (")	μ	Δt (days)
C	M1	-1.717	-1.697	10.76	$\equiv 0$
B	M2	-2.334	0.612	11.92	0.25
A	S1	-2.305	-0.577	-19.68	1.22
D	S2	0.796	0.315	-0.99	120.08

NOTE. — Similar to Table 1, but for our sample cusp lens similar to RX J1131–1231. We again introduce new image labels such that M1 is the leading minimum, M2 is the trailing minimum, S1 is the leading saddle, and S2 is the trailing saddle.

simply rescale the time delays through the lensing time scale t_0 .

2. METHODS

2.1. Reference smooth lens

We examine the effects of substructure by comparing the properties of images produced by a galaxy with substructure to those produced by an equivalent smooth galaxy. We model the smooth galaxy using a pseudo-Jaffe profile with scaled surface mass density

$$\kappa_{\text{tot}}(r) = \frac{\Sigma(r)}{\Sigma_{\text{crit}}} = \frac{b_{\text{tot}}}{2} \left(\frac{1}{r} - \frac{1}{\sqrt{a^2 + r^2}} \right), \quad (2)$$

where $\Sigma_{\text{crit}} = (c^2 D_s)/(4\pi G D_l D_{ls})$ is the critical surface density for lensing, where D_l , D_s , and D_{ls} are angular diameter distances between the observer and lens, the observer and source, and the lens and source, respectively. We have written the equation for a circular lens, but it is straightforward to obtain an elliptical model by replacing r with an appropriate elliptical radius. The pseudo-Jaffe model is equivalent to the singular isothermal model for $r \ll a$, but the density falls more quickly at large radii $r \gg a$ to keep the total mass finite, $M_{\text{tot}} = \pi a b \Sigma_{\text{crit}}$. The scale radius a can therefore be thought of as a sort of truncation radius, although the truncation is not sharp. We set a to be 300 kpc, although the particular choice has little effect on our results provided it is well outside the Einstein radius (see Section 2.4 for more discussion). The parameter b_{tot} is the Einstein radius of the lens.

We calibrate the pseudo-Jaffe model by fitting it to observed lens systems. The fit is not quantitatively precise because we model the lens environment using a simple external tidal shear, when in truth the lens may lie in a group of galaxies that has a more complicated effect (e.g., Kundić et al. 1997; Momcheva et al. 2006). For the present work, we seek only to obtain reasonable smooth mass models, not to replicate any observed lens in rich detail.

We create a lens with a “fold” image configuration similar to that of PG 1115+080 (Weymann et al. 1980). The lens galaxy redshift is $z_l = 0.31$ and the source redshift is $z_s = 1.72$, so the lensing time scale is $t_0 = 46.5$ days (see Equation (1)). Our reference smooth model is circular with Einstein radius $b_{\text{tot}} = 1''.16$, and it has external shear $\gamma = 0.12$ at position angle $\theta_\gamma = 65^\circ$ (east of north). We place a source at position $(-0''.032, 0''.118)$ relative to the center of the galaxy, and obtain the four images listed in Table 1 and shown in Figure 1 below.

We also create a lens with a “cusp” image configuration similar to that of RX J1131–1231 (Sluse et al. 2003). The lens redshift is $z_l = 0.295$ and the source redshift is $z_s = 0.658$, yielding a lensing time scale $t_0 = 45.5$ days. Our reference smooth model has Einstein radius $b_{\text{tot}} = 1''.85$, ellipticity

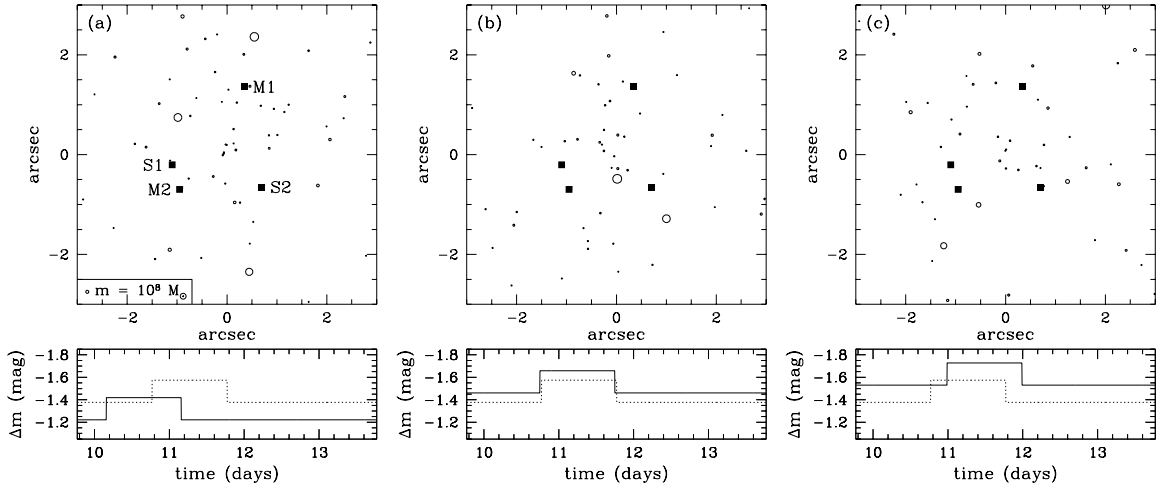


FIG. 1.— Upper panels: the squares show the images for our sample fold configuration (compare with Table 1). In terms of the traditional image labeling for PG 1115+080, we have M1=C, M2=A₁, S1=A₂, and S2=B. Circles show the Einstein radii of mass clumps; panel (a) includes a key with $m = 10^8 M_\odot$ for reference. The three panels show random realizations of a substructure population in which the substructure mass fraction is $f_s = 0.01$, and the subhalo mass function is $dN/dm \propto m^{-1.8}$ over the range 10^7 – $10^9 M_\odot$. Lower panels: sample light curves for image M2. In these examples, we assume image M1 brightens by 20% at $t = 0$ and returns to its original flux at $t = 1$ day. We plot the magnitude difference $\Delta m = m_{M2} - m_{M1}$. In each panel the dotted curves shows the light curve for the reference smooth model, while the solid curve shows the actual light curve for the specific realization of substructure. Notice that the substructure perturbs both the flux ratio and time delay of image M2 relative to image M1. (The results for other images are similar.)

$e = 0.16$ at position angle $\theta_e = -56^\circ$ (east of north), and external shear $\gamma = 0.12$ at position angle $\theta_\gamma = -83^\circ$. We place a source at position $(-0.''549, -0.''142)$ relative to the center of the galaxy, and obtain the four images listed in Table 2 and shown in Figure 9. While there are quantitative differences in the time delays between the fold and cusp lens examples, many of the scalings and conceptual conclusions remain the same. Therefore in most of the presentation we focus on the fold lens for clarity. The exceptions are discussed in Section 3.5.

We should comment on our labeling of the lensed images. Images are traditionally labeled by letters (e.g., A, B, C, D) using criteria chosen by the discoverers; different criteria have been used, with the result that existing labels are not very informative. Saha & Williams (2003) instead advocate labeling the images 1–2–3–4 in arrival-time order, arguing that this labeling is robust (at least for smooth mass distributions; see Section 3.5), and presenting rules for using the image configuration to determine the labels. We assert that it is useful to have labels convey not only the time ordering but also the type of image as well. We therefore use “M” or “S” to indicate (respectively) an image at a local minimum or saddlepoint of the time delay surface, combined with “1” or “2” to indicate (respectively) the leading or trailing image of each type. Thus, the four images arranged in arrival-time order are M1, M2, S1, and S2. In Tables 1 and 2 we give the correspondence between our labeling scheme and the traditional letter labels for PG 1115+080 and RX J1131–1231.

2.2. Subhalo population

While detailed semi-analytic substructure models are now available (e.g., Taylor & Babul 2001, 2004; Benson et al. 2002; Zentner & Bullock 2003; Koushiappas et al. 2004; Oguri & Lee 2004; van den Bosch et al. 2005; Zentner et al. 2005), for pedagogical purposes it is attractive to adopt simple but reasonable assumptions about the mass function and spatial distribution of subhalos (e.g., Metcalf & Madau 2001;

Chiba 2002; Dalal & Kochanek 2002; Metcalf et al. 2004).² We assume that subhalos trace the total mass distribution, so the average surface mass density in subhalos at radius r is $\kappa_s(r) = f_s \kappa_{\text{tot}}(r)$, where f_s is the substructure mass fraction.

CDM simulations predict that the subhalo mass function is approximately a power law, $dN/dm \propto m^\beta$ with $\beta \approx -1.8$ (e.g., Ghigna et al. 2000; Helmi et al. 2002; Gao et al. 2004; Diemand et al. 2007). In order to explore how subhalo masses affect time delays, we consider masses in some finite range $m_1 \leq m \leq m_2$. The mean subhalo mass is

$$\langle m \rangle = \frac{1 + \beta}{2 + \beta} \frac{m_2^{2+\beta} - m_1^{2+\beta}}{m_2^{1+\beta} - m_1^{1+\beta}}. \quad (3)$$

Equivalently, we may write the lower mass limit in terms of the mean mass and dynamic range $q = m_2/m_1$ as

$$m_1 = \langle m \rangle \frac{2 + \beta}{1 + \beta} \frac{q^{1+\beta} - 1}{q^{2+\beta} - 1}. \quad (4)$$

Another quantity that will prove to be useful is the mean squared mass,

$$\langle m^2 \rangle = \langle m \rangle^2 \frac{q^{1+\beta} - 1}{1 + \beta} \frac{q^{3+\beta} - 1}{3 + \beta} \left(\frac{2 + \beta}{q^{2+\beta} - 1} \right)^2. \quad (5)$$

When $q = 1$ the mass function reduces to a Dirac δ -function and all subhalos have the same mass.

Figure 1 shows three realizations of a subhalo population in which the substructure mass fraction is $f_s = 0.01$ and the subhalos have masses between $m_1 = 10^7$ and $m_2 = 10^9 M_\odot$. For reference, this mass function has $\langle m \rangle = 6.2 \times 10^7 M_\odot$ and $\langle m^2 \rangle / \langle m \rangle = 2.8 \times 10^8 M_\odot$.

2.3. Subhalo models

² A few microlensing studies have worked directly with N -body simulations, but both the original simulations and the lensing calculations are computationally expensive (Bradač et al. 2002, 2004; Amara et al. 2006; Macciò et al. 2006).

For a subhalo of mass m , it is useful to define a scaled mass

$$\hat{m} \equiv \frac{m}{\Sigma_{\text{crit}}} = \pi R_{\text{Ein}}^2, \quad (6)$$

which has dimensions of area. Here R_{Ein} is the Einstein radius of the subhalo if it is a point mass. In most of our analysis we do treat subhalos as point masses for simplicity. The lens potential of a subhalo is then

$$\phi = \frac{\hat{m}}{\pi} \ln r, \quad (7)$$

while the deflection angle is

$$\alpha = \frac{d\phi}{dr} = \frac{\hat{m}}{\pi r}. \quad (8)$$

We also consider subhalos modeled as truncated isothermal spheres. The truncation occurs in the three-dimensional density profile, so we have $\rho \propto r^{-2}$ out to the truncation radius r_t , and $\rho = 0$ for $r > r_t$. The lensing deflection angle works out to be

$$\begin{aligned} r < r_t : \alpha &= \frac{\hat{m}}{\pi r} \left[1 - \left(1 - \frac{r^2}{r_t^2} \right)^{1/2} + \frac{r}{r_t} \cos^{-1} \left(\frac{r}{r_t} \right) \right], \\ r > r_t : \alpha &= \frac{\hat{m}}{\pi r}. \end{aligned} \quad (9)$$

It is straightforward to obtain the potential by integrating, $\phi = \int \alpha dr$, but it is not instructive to write the (somewhat long) expression here.

2.4. Calculations

To obtain a mass model with substructure, we leave a fraction $(1 - f_s)$ of the dark matter mass in a smooth component, and replace a fraction f_s with subhalos. The expected number of subhalos is

$$\langle N \rangle = \frac{f_s M_{\text{tot}}}{\langle m \rangle} = \frac{\pi a b_{\text{tot}} f_s}{\langle \hat{m} \rangle}, \quad (10)$$

and we draw the actual number from a Poisson distribution with this mean. The subhalo positions are assigned randomly as follows. For the pseudo-Jaffe model the cumulative probability distribution for the radius is

$$P_r(r) = \frac{\int_0^r r' \kappa_s(r') dr'}{\int_0^\infty r' \kappa_s(r') dr'} = 1 + \frac{r}{a} - \left(1 + \frac{r^2}{a^2} \right)^{1/2}. \quad (11)$$

We pick a random value for P_r uniformly between 0 and 1, and then invert Equation (11) to find the random radius. The explicit inversion is

$$r = a \frac{P_r(2 - P_r)}{2(1 - P_r)}. \quad (12)$$

(Again, these equations are for a circular lens, but the extension to an elliptical mass distribution is straightforward.) We then pick a random azimuthal angle uniformly between 0 and 2π .

The pseudo-Jaffe model formally extends to infinity, but we do not actually need to consider subhalos at large radii because they have little effect on the time delays. In the Appendix, Equation (A13) allows us to calculate the rms error that we make on time delays if we neglect subhalos beyond some radius R_0 . We use this equation to set the threshold

radius to ensure that our time delay errors are less than 0.001 days. The fact that time delays are not very sensitive to distant subhalos is the reason that our results do not depend strongly on the choice of the pseudo-Jaffe ‘‘truncation’’ radius.

The subhalo masses are assigned randomly from the power law mass function. The cumulative probability distribution for the mass is

$$P_m(m) = \frac{m^{1+\beta} - m_1^{1+\beta}}{m_2^{1+\beta} - m_1^{1+\beta}}. \quad (13)$$

We pick a random value for P_m uniformly between 0 and 1, and invert Equation (13) to find the random mass. (When the mass function is a δ -function, all halos have the same mass and this process is unnecessary.)

The number of subhalos in a simulation varies between a few hundred and a few hundred thousand, depending on the subhalo masses and the substructure mass fraction. We use a tree algorithm (Barnes & Hut 1986) to compute the net lensing potential, deflection, and magnification quickly and efficiently. All of this analysis is included in an updated version of the public software package *gravlens* (Keeton 2001).

To find the images as they are affected by substructure, we note that the shifts in the image positions are small (e.g., Chen et al. 2007), so it is efficient to start from the smooth images and perturb the positions iteratively:

$$x^{(i+1)} = x^{(i)} + \mu^{(i)} \cdot \delta u^{(i)}, \quad \delta u^{(i)} = x^{(i)} - \alpha^{(i)} - u, \quad (14)$$

where $\alpha^{(i)}$ and $\mu^{(i)}$ are the deflection vector and magnification tensor, respectively, evaluated at the current position $x^{(i)}$. (Here i labels the iteration step, not the image index.) Note that $x^{(i)} - \alpha^{(i)}$ represents the source position associated with the current image position, so $\delta u^{(i)}$ is the offset in the source plane. When the image position correctly solves the lens equation, $\delta u^{(i)}$ vanishes and the iteration process converges.

A massive clump near one of the ‘‘macro-images’’ can in principle split it into several ‘‘milli-images’’.³ We check for this possibility by comparing the parity of the recovered image against the parity of the reference image. If we start with a minimum but recover a saddle (or vice versa), we know there are extra images and we have found one. Note that if we start with a minimum and recover a minimum (or likewise for a saddle), that does not prove there are no extra images. However, we use the minimum/saddle cases to estimate the fraction of simulations that yield extra images, and find it to be small. We throw away the small number of simulations that yield extra images.

Once we have found the image positions, we use Equation (1) to compute the differential time delay between image pairs, $\Delta t_{ij} = \tau(x_j) - \tau(x_i)$.

3. RESULTS

3.1. Time delay perturbations

We begin by examining our sample fold lens in the presence of substructure, as shown in Figure 1. In the bottom row of that figure we show sample light curves for image M2 (assuming for pedagogical purposes a simple square wave variation in the source); the results for the other images are similar.

³ With point mass clumps, or indeed any clump with a cuspy central density steeper than $\Sigma \propto r^{-1}$, there is formally a ‘‘micro-image’’ very close to each clump. However, these images are highly demagnified and hence unimportant. They are absent when the clump central density is shallower than $\Sigma \propto r^{-1}$.

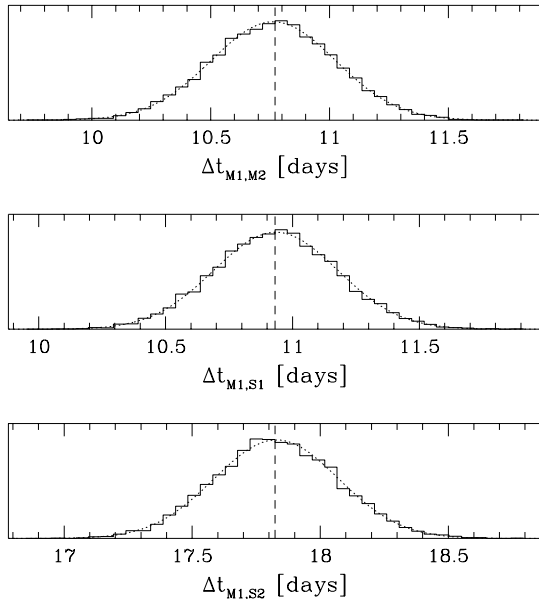


FIG. 2.— Histograms of the time delays between the images, for 10^4 Monte Carlo simulations with substructure mass fraction $f_s = 0.01$ and subhalo mass $m = 10^8 M_\odot$. (The vertical axis scale is arbitrary.) The vertical lines indicate the time delays for the reference smooth model. Superposed on each histogram is a Gaussian (dotted line) with the same mean and variance as the simulated data.

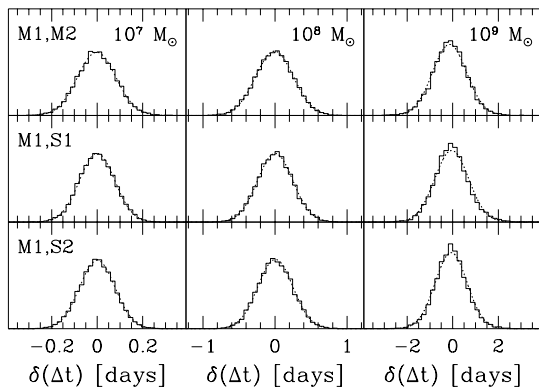


FIG. 3.— Histograms of the time delays between different images (rows), for different values of the subhalo mass (columns). We now plot $\delta(\Delta t)$, the difference between the time delay with substructure and the delay for the reference smooth model. All cases have 10^4 Monte Carlo simulations with a substructure mass fraction $f_s = 0.01$. Notice that the horizontal scale varies from one column to the next. (The vertical axis scale varies as well, but the units are arbitrary anyway.) Equivalent Gaussians are again shown with dotted lines.

The substructure clearly changes both the flux ratio and time delay between the images. In these examples, the flux ratio is perturbed by 0.1–0.2 mag and the time delay is perturbed by some fraction of a day. Oguri (2007) also showed (in less detail) that substructure can affect lens time delays, but he focused on this as a source of noise in lensing measurements of the Hubble constant. We instead propose that time delay perturbations provide a new way to detect and study substructure itself, if lens time delays can be measured well enough.

The remainder of the paper is devoted to exploring how time delay perturbations depend on the subhalo population. To that end, we start with a simple case in which all the subhalos are point masses with $m = 10^8 M_\odot$, and the substructure mass fraction is $f_s = 0.01$. For each substructure real-

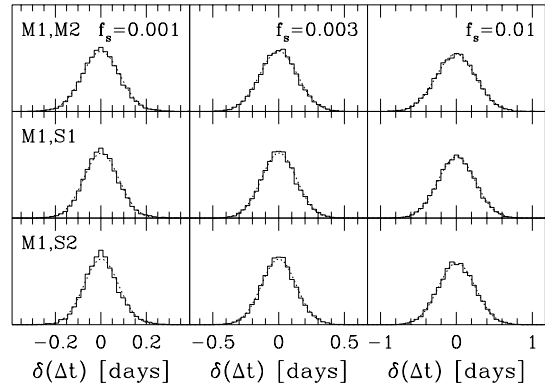


FIG. 4.— Similar to Figure 3, but for different values of the substructure mass fraction. All simulations have subhalos with mass $m = 10^8 M_\odot$.

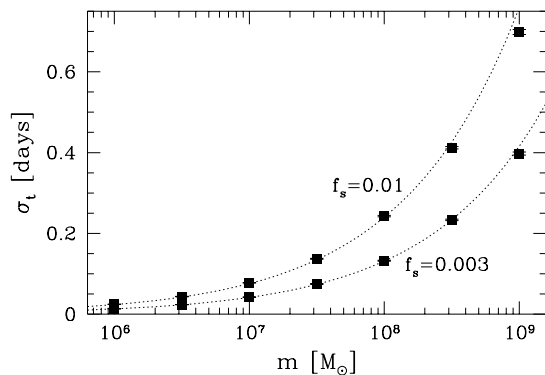


FIG. 5.— Time delay scatter as a function of subhalo mass. The points show results from Monte Carlo simulations (compare Figures 3 and 4), with statistical errorbars from bootstrap resampling. The dotted curves show the scaling $\sigma_t \propto (f_s m)^{1/2}$ from Equation (A10) in the Appendix (after we fit for the proportionality constant using the $f_s = 0.01$ points).

ization we compute the time delays between the images; we then repeat the process 10^4 times and make histograms of the time delays, as shown in Figure 2. For each image pair, the average time delay matches the prediction of the reference smooth model very well, which makes sense because the smooth model can be thought of as an average over the subhalo population. These three time delay histograms appear to be Gaussian. (The histogram of the time delay between the close images M2 and S1 is somewhat different, as discussed in Section 3.5.) We attribute the Gaussianity to the Central Limit Theorem: the lens potential is a sum of many random terms, and such a sum tends toward a Gaussian distribution if the mean and variance of each term are finite, which we verify in the Appendix.⁴ The standard deviation is $\sigma_t = 0.24$ – 0.26 days for all three image pairs shown in Figure 2.

3.2. Subhalo mass and substructure mass fraction

Next we consider the effects of changing the subhalo mass (Figure 3) and the substructure mass fraction (Figure 4). In order to place different image pairs on a common scale, we plot histograms of the time delay perturbation $\delta(\Delta t)$, defined to be the difference between the time delay with substructure and the time delay for the reference smooth model. All of the histograms appear to be nicely Gaussian, to be centered on

⁴ The Central Limit Theorem has not been used in millilensing before, because it does not obviously apply to flux ratios. See the Appendix for more discussion.

zero, and to have widths that increase with both the subhalo mass and the substructure mass fraction.

We can quantify this last point by plotting the time delay scatter σ_t as a function of the subhalo mass, for different values of the substructure mass fraction, as shown in Figure 5. In the Appendix we use the Central Limit Theorem to make an initial prediction of the scaling of the time delay scatter (see Equation (A10)):

$$\sigma_t \propto (f_s m)^{1/2}. \quad (15)$$

To test this prediction, we use the results from simulations with $f_s = 0.01$ to fit for the proportionality constant, and then plot the analytic curves alongside the simulation results in Figure 5. The agreement is striking given the simplicity of the analytic prediction. Strictly speaking, the analytic scaling appears to overestimate the time delay scatter when the subhalo mass is large. We can identify at least two possible explanations. First, when f_s is fixed increasing the subhalo mass decreases the number of subhalos, which may make the Central Limit Theorem less applicable and invalidate an approximation in Equation (A6). Second, as the subhalo mass increases the perturbations to the image positions also increase, which may invalidate one of our starting assumptions in the Appendix. We are working on a more sophisticated theory of time delay perturbations to address both issues. For now, though, we consider the success of the initial analytic prediction to be very encouraging.

The scaling of the time delay scatter with subhalo mass has an important corollary: there is no measurable effect on time delays from low-mass objects, such as stars. This means we can study millilensing at any wavelength without ‘‘contamination’’ from microlensing.

3.3. Subhalo mass function

So far we have assumed that all subhalos have the same mass; now we consider a power law mass function. Figure 6 shows the time delay scatter as a function of the dynamic range $q = m_2/m_1$ and power law slope β of the mass function. The dynamic range has a significant effect: the broader the mass function, the more scatter there is in lens time delays. The power law slope affects the time delay scatter as well, but much more modestly. For comparison we also plot the analytic scaling from Equation (A9) in the Appendix,

$$\sigma_t \propto \left(f_s \frac{\langle m^2 \rangle}{\langle m \rangle} \right)^{1/2}, \quad (16)$$

where the ratio $\langle m^2 \rangle / \langle m \rangle$ can be found from Equation (5). The analytic formula does not match the simulation results perfectly, but it seems remarkably good for something so simple. We take this as an indication that the theory of time delay millilensing will be analytically tractable. Having a rigorous theory of millilensing is possible only with time delays; analytic results for flux ratio millilensing are elusive because flux ratios are highly nonlinear and the Central Limit Theorem does not apply (see the Appendix).

3.4. Internal structure of subhalos

So far we have treated the mass clumps as point masses, partly for simplicity and partly because we know the gravity outside any spherical mass clump is the same as that of a point mass. However, dark matter subhalos in general have some spatial extent, and if they overlap lensed images this may

be important for millilensing. In this pilot study we mainly want to determine when the point mass approximation is reasonable and when we need to worry about subhalo size and structure. We therefore consider a simple model of isothermal spheres that are truncated (in three dimensions) at some radius r_t . Figure 7 shows how the time delay scatter changes when we vary the truncation radius while keeping the subhalo mass fixed. (The key scale is the dimensionless truncation radius, $\hat{r}_t = r_t/R_{\text{Ein}}$, where R_{Ein} is the Einstein radius of a point mass with the same mass, as defined by Equation (6).)

Depending on the mass, subhalos need to extend beyond 10 or more Einstein radii before the internal structure becomes important. The obvious next step is to model tidal truncation and estimate the sizes of realistic subhalos. There are some important effects to consider: tidal forces vary with position in the parent halo; and tidal truncation also corresponds to mass loss (so, strictly speaking, it is not right to vary the truncation radius while keeping the subhalo mass fixed, although that is a useful pedagogical exercise). These effects are incorporated into semi-analytic substructure models, so in follow-up work we will study time delay millilensing using realistic subhalo populations drawn from those models.

3.5. Arrival-time ordering of lensed images

Saha & Williams (2003) suggested that the arrival-time ordering of lensed images is a robust prediction of smooth lens models (at least, those with relatively simple angular structure). With the help of a few simple rules, they noted, it is usually easy to identify the two minima and two saddlepoints in a quad lens, and then to deduce the arrival-time ordering. If the situation is not immediately obvious, a simple lens model makes it clear. We have therefore chosen to use the image classification and ordering as the basis of our labeling scheme: in arrival-time order we have the leading minimum (M1), the trailing minimum (M2), then the leading saddle (S1), and finally the trailing saddle (S2).

In the fold image configuration we have considered, substructure does not affect the arrival-time ordering. The reason is that the time delay perturbations are small compared with most of the time delays themselves. It might seem that the close image pair M2/S1 could provide an exception, because the smooth model time delay (0.16 day) is shorter than some of the substructure perturbations we have seen. However, by definition a saddlepoint in the time delay surface must be higher than a nearby local minimum, so image S1 must trail M2 and the overall ordering must be preserved. One consequence is that the histogram for the M2/S1 time delay cannot remain Gaussian as the substructure perturbations grow, as shown in Figure 8. This implies that the substructure influences both images at some level, although the $\Delta t_{M2,S1}$ histograms are broad enough that it seems fair to say that substructure affects even nearby images quite differently. The only way this general analysis can be violated is if a massive and concentrated clump lies close enough to images M2 and S1 to change the global topology of the time delay surface; but such a situation would be immediately apparent from the image configuration (see Saha & Williams 2003).

The issue of arrival-time ordering is strikingly different for a cusp image configuration like that in RX J1131–1231. Figure 9(a) shows the images along with selected arrival-time contours for our smooth mass model. In this example, and indeed in all smooth models of RX J1131–1231 examined by Morgan et al. (2006), the image labeled M1 is the leading image. However, as shown in Figure 9(b), substructure can re-

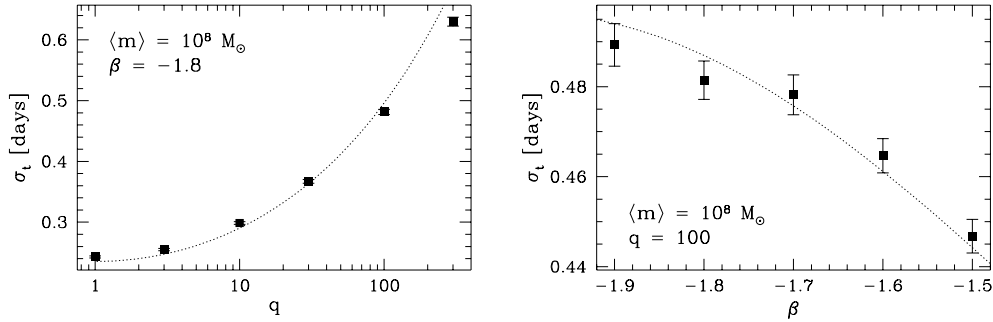


FIG. 6.— Dependence of the time delay scatter on the subhalo mass function. The mass function is a power law, $dN/dm \propto m^\beta$, over the range $m_1 \leq m \leq m_2$. The two panels show σ_t as a function of the dynamic range $q = m_2/m_1$ and the power law slope β . The points show results from 10^4 Monte Carlo simulations, with bootstrap errorbars. The dotted lines show the scalings predicted by Equation (A9) in the Appendix (after we fit for the proportionality constant). The substructure mass fraction is $f_s = 0.01$.

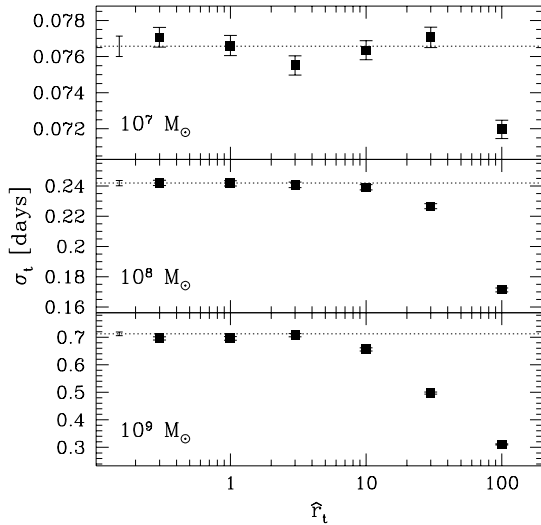


FIG. 7.— Time delay scatter for subhalos modeled as truncated isothermal spheres, as a function of the dimensionless truncation radius $\hat{r}_t = r_t/R_{\text{Ein}}$. The dotted lines (with errorbars) show the results for point mass subhalos for comparison. The three panels show different subhalo masses; the substructure mass fraction is $f_s = 0.01$ in each case. We show results for the M1/S2 image pair, but the results for other pairs are similar.

verse the arrival-time order of the images M1 and M2, such that the overall ordering is M2/M1/S1/S2. In terms of the topology of the time delay surface, we can still say the saddlepoint must be higher than the two minima on either side, so S1 must trail both M1 and M2. However, there are no such restrictions on the heights (or depths, equivalently) of the two minima with respect to each other. It is fairly easy for substructure to modify one or both of the minima enough to change their relative heights, and hence the arrival-time ordering of images M1 and M2. In fact, some 27% of realizations with modest substructure (substructure mass fraction $f_s = 0.01$ and subhalo mass $m = 10^8 M_\odot$) predict an arrival-time reversal (see Figure 10).

We believe image reversal by substructure may already have been observed in RX J1131–1231, based on the time delays reported by Morgan et al. (2006). The time ordering observed among the three bright images is M2/M1/S1⁵ with $\Delta t_{M2,M1} = 2.20^{+1.55}_{-1.64}$ days, $\Delta t_{M2,S1} = 11.98^{+1.52}_{-1.27}$ days, and $\Delta t_{M1,S1} = 9.61^{+1.97}_{-1.57}$ days. These time delays present two puzzles. First, image M2 is observed to lead image M1, whereas

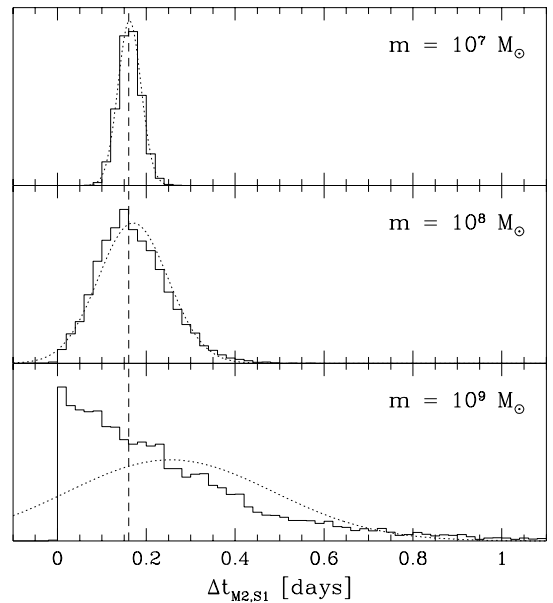


FIG. 8.— Histograms of the time delay of the close image pair M2/S1 for our sample fold lens (compare Figs. 2 and 3). The substructure mass fraction is $f_s = 0.01$, and the subhalo mass is indicated in each panel. The vertical lines indicate the time delay for the reference smooth model. Superposed on each histogram is a Gaussian (dotted line) with the same mean and variance as the simulated data.

smooth models predict the opposite. Second, the observed M2/S1 and M1/S1 time delays are an order of magnitude longer than predicted by smooth models. Morgan et al. (2006) focused their attention on the second problem, and showed that placing a single, massive ($\gtrsim 5 \times 10^{10} M_\odot$) subhalo near image S1 could explain the long M2/S1 time delay. Their models still predicted M1 to be the leading image, though.

As we have demonstrated, a *population* of subhalos might be able to reverse the ordering to make M2 the leading image. It will still take a lot of modeling to draw quantitative conclusions about the substructure required to explain the image ordering and the long time delays; we will present the modeling details elsewhere (C. R. Keeton & L. A. Moustakas, in preparation). For now, we mainly want to introduce the idea that the temporal ordering of images in a cusp configuration can be changed by substructure—and that this effect may already have been observed.

⁵ We have switched to our labeling scheme using the identifications M1=C, M2=B, S1=A, and S2=D.

3.6. Macromodel uncertainties

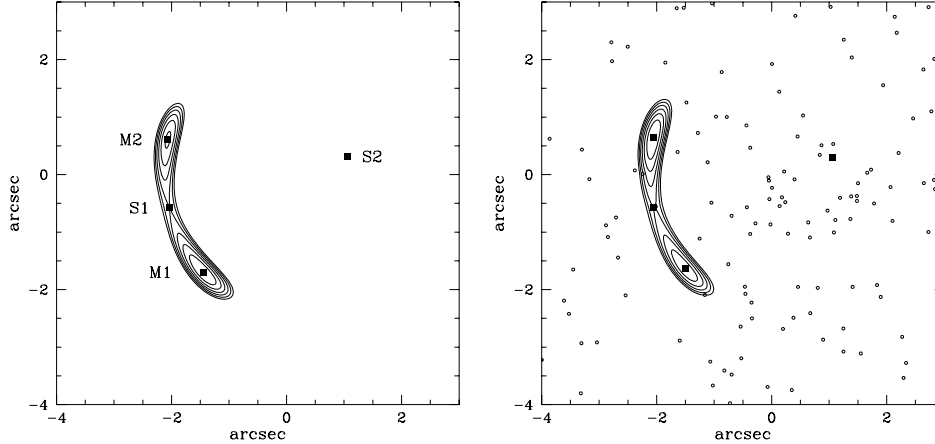


FIG. 9.— (a) Image configuration for our sample cusp lens, assuming a smooth mass distribution (compare with Table 2). In terms of the traditional image labeling for RX J1131–1231, we have M1=C, M2=B, S1=A, and S2=D. Positions are measured with respect to the center of the lens galaxy at (0,0). Selected contours of constant arrival time are also shown. Counting contours shows that the minimum containing image M2 is shallower than the minimum containing image M1, hence M2 trails M1. (b) Example of the same lens with substructure (with $f_s = 0.01$ and $m = 10^8 M_\odot$). Now it is apparent that the minimum containing the image labeled M2 is actually deeper than the minimum containing M1. In other words, substructure has reversed the arrival-time ordering of these two images such that M2 actually precedes M1. The ordering of S1 and S2 remains unchanged. (Note that the contour levels are different in the two panels; they are chosen to best reveal the minima and saddlepoint in each case.)

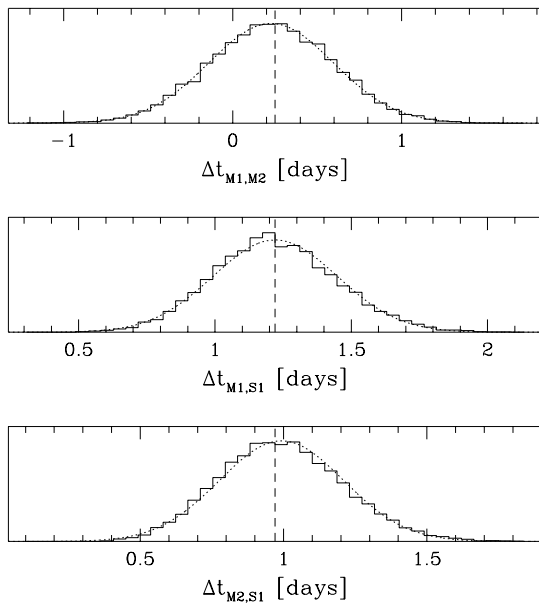


FIG. 10.— Histograms of the time delays between the close images in our example cusp lens. The images labeled M1 and M2 lie at minima of the time delay surface, while S1 lies at a saddlepoint. In smooth models the image ordering is always M1/M2/S1/S2. However, in Monte Carlo simulations with a substructure mass fraction $f_s = 0.01$ and subhalo mass $m = 10^8 M_\odot$, about 27% of the realizations have $\Delta t_{M1,M2} < 0$ which means image M2 actually leads image M1. In such cases the overall ordering in M2/M1/S1/S2. As usual, vertical lines indicate the time delays for the reference smooth model, and a comparison Gaussian is superposed on each histogram.

Having shown that substructure affects lens time delays, we still need to consider how well the perturbations could be detected in observed lenses. The question is whether uncertainties in the “macromodel” used to characterize the smooth component of the lens mass distribution could mask the effects of substructure. One key concern is the radial profile degeneracy: especially in quad lenses, varying the radial density profile of the lens galaxy can rescale the time delays while leaving other observables unchanged (e.g., Falco et al. 1985; Keeton & Kochanek 1997; Saha 2000; Kochanek 2002). At

first glance, this would seem to make changes induced by substructure degenerate with changes in the radial profile.

However, the radial profile rescaling affects all images in the same way, while substructure affects each image differently. So with more than one time delay (as in a quad lens), ratios of the delays cancel the rescaling and isolate substructure effects, as shown in Figure 11. The radial profile degeneracy will therefore not be a fundamental limitation in attempts to probe substructure with time delays. This very promising inference is currently empirical, but we expect it can be made rigorous with a full theory of time delay millilensing. Since radial profile effects do not cancel perfectly (there are small differences in the widths of the time delay ratio histograms in Figure 11), the theory will also be useful in understanding and correcting for these residual effects.

Another source of uncertainty is the angular structure of the macromodel. While it is common to fit observed lenses with an ellipsoidal mass distribution and external shear (and we have used such a model to construct our mock lenses), real galaxies may be more complex. In particular, observed (e.g., Bender et al. 1989; Saglia, Bender & Dressler 1993; Rest et al. 2001) and simulated (e.g., Heyl, Hernquist & Spergel 1994; Naab & Burkert 2003; Jesseit et al. 2005; Naab et al. 2006) elliptical galaxies often contain mild departures from elliptical symmetry that can be described with $m = 3$ and $m = 4$ multipole terms in the surface mass density. Evans & Witt (2003) suggested that such multipole terms might provide an alternative to clumpy substructure when fitting observed lenses. Although multipoles turn out not to provide a satisfactory explanation of observed flux ratio anomalies (Kochanek & Dalal 2004; Congdon & Keeton 2005; Yoo et al. 2005, 2006), it is important to consider how they might influence the analysis of time delays.

We can do this by taking our mock lenses generated with substructure and trying to fit them with multipole models. For this exercise we adopt $0''.003$ errorbars for the image positions, which is typical of observations with the *Hubble Space Telescope* (*HST*) and radio interferometry, and 5% time delay uncertainties, which is similar to the precision achieved

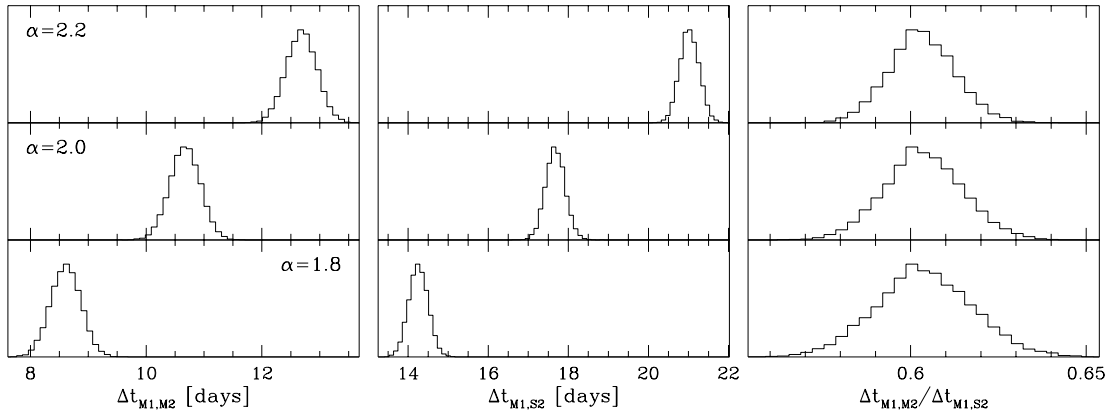


FIG. 11.— Examining the radial profile degeneracy in our mock fold lens. The smooth mass component has a power-law density profile $\rho \propto r^{-\alpha}$, or equivalently a surface density profile $\kappa \propto R^{1-\alpha}$, while the substructure is still given by our pseudo-Jaffe model. Varying the profile rescales the time delays (left and middle columns). However, the time delay *ratio* (right column) is largely unaffected: the mean ratio stays the same, while there is a small change in the scatter. (The time delays between images M1, M2, and S2 are used for illustration; time delays involving image S1 could be used as well.) Time delay ratios therefore allow us to probe dark matter substructure without worrying about the radial profile degeneracy.

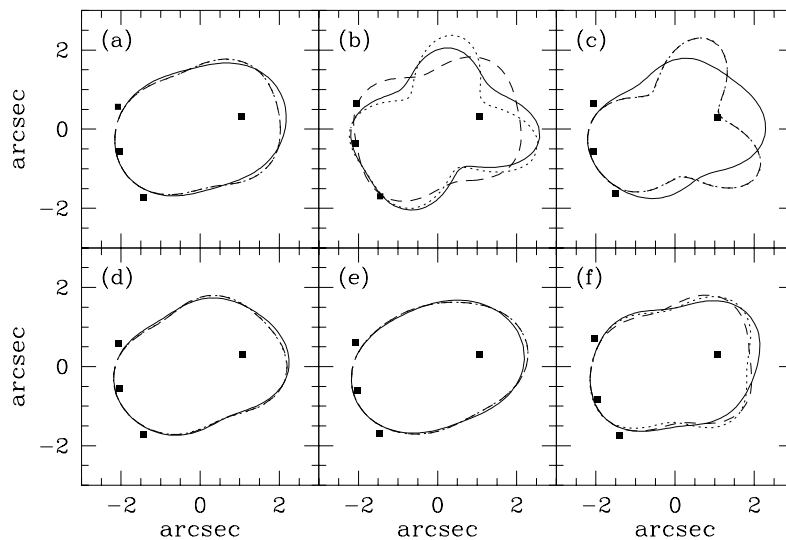


FIG. 12.— Lensing critical curves for multipole models fit to six random mock lenses. We fit the image positions and time delays using multipole terms that are unconstrained (dotted curves) or have Gaussian priors (solid curves; see text). We also consider adding the image flux ratios as constraints (dashed curves). Among these lenses, cases b and c are the most glaring examples of failed multipole models; cases d and f are less dramatic but failures nonetheless.

for quad lenses today (see the compilation by Oguri 2007). In general, we find that multipole models can formally provide a good fit to the image positions and time delays, but many of the models have unreasonably large multipole terms that lead to unrealistic galaxy shapes, as shown in Figure 12. To avoid the unreasonable models we can impose some priors on the multipole terms. Since the multipole moments in observed and simulated elliptical galaxies are typically at the percent level, a simple first step is to adopt Gaussian priors on the multipole amplitudes a_3 and a_4 with a mean of zero and standard deviation of 0.02. (In the present analysis we do not impose any constraints on the orientations of the multipole terms.) With these mild amplitude priors, multipole models fail (i.e., they are inconsistent with the data at more than 95% confidence) for 27 of the 100 mock lenses we examine. We are in the process (J. van Saders et al., in preparation) of deriving more sophisticated priors on multipole terms from a large sample of galaxies in the Galaxy Evolution from Morphologies and SEDs survey (GEMS; Rix et al. 2004), and we expect that those will be even more valuable in constraining

macromodels and thus aiding the identification of time delay anomalies.

It is perhaps artificial to insist that we must identify anomalous lenses on the basis of time delays alone, when flux ratios are also available to provide additional constraints. If we fit the flux ratios along with the image positions and time delays, we find that multipole models fail (at 95% confidence) for 52 of 100 mock lenses even if we use generous 10% flux errorbars and do not impose any priors on the multipole terms. Interestingly, only 28 of those failures would be identified on the basis of flux ratios alone; in 24 of the mock lenses, it is only when we fit the time delays and flux ratios simultaneously that the anomalies become clear. We infer that time delays and flux ratios contain different and complementary information about the small-scale structure of the lens potential.

While we plan to address the issues of multipole priors and complementarity of time delays and flux ratios in detail in future work, we offer the preliminary conclusion that macromodel uncertainties can be controlled well enough that we can expect to use time delays to learn about substructure.

4. DISCUSSION AND CONCLUSIONS

We have shown that substructure in lens galaxies modifies the time delays in multiply-imaged gravitational lenses. The amplitude of time delay perturbations depends on the abundance of substructure, the mass function of subhalos, and to some extent the internal structure of subhalos as well. This phenomenon, which we call time delay millilensing, has some very attractive properties. First, the effects of substructure on time delays are fairly easy to understand, both conceptually and quantitatively. Second, time delay perturbations are unaffected by stellar microlensing or extinction in the lens galaxy. Third, time delay ratios are immune to the radial profile degeneracy in lens modeling.

Furthermore, time delay millilensing is sensitive to the mass function of subhalos in a different way than flux ratio and astrometric millilensing. For point mass perturbers, the lensing optical depth depends on $\int R_{\text{Ein}}^2 (dN/dm) dm \propto \int m (dN/dm) dm$. The potential of a clump scales with its mass, so time delay perturbations depend in full on $\int m^2 (dN/dm) dm$. (See the Appendix for more details.) For comparison, position perturbations have a scale of $R_{\text{Ein}} \propto m^{1/2}$ while magnification perturbations are dimensionless, which means that astrometric millilensing depends on $\int m^{3/2} (dN/dm) dm$ while flux ratio millilensing depends on $\int m (dN/dm) dm$ (compare Dalal & Kochanek 2002; Dobler & Keeton 2006; Chen et al. 2007; Shin & Evans 2008).

We therefore suggest that lens time delays should join image positions and flux ratios as tools for studying dark matter substructure in distant galaxies. Since the three observables measure different moments of the subhalo mass function, the combination of all three will ultimately provide a powerful way to test CDM predictions and even to explore the nature of dark matter itself, given that different dark matter candidates may produce different mass functions at subgalactic scales, as a function of lens galaxy mass and redshift.

Before we try to use time delays to measure substructure, it is vital that we understand whether systematic uncertainties in lens models could corrupt substructure constraints. We have explicitly shown that the radial profile degeneracy is not a significant problem, as time delay ratios essentially factor out the profile dependence. We have drawn the preliminary conclusion that uncertainties in the angular structure of the lens potential can be dealt with, using additional flux ratios data and/or independent constraints on the shapes of galaxy mass distributions. Other potential concerns may include the environment of the lens galaxy (Keeton & Zabludoff 2004), and (sub)structure along the line of sight (Keeton 2003; Chen et al. 2003; Metcalf 2005a,b; Lieu 2008). For all of these issues, the important point is again that non-local features in the lens potential affect the images in some coordinated way, whereas substructure affects the images differently.

We also need to predict time delay perturbations for subhalo populations that are more realistic than the simple ones we have used (for pedagogical purposes) here. This work is underway, using existing semi-analytic substructure models. By incorporating important physical effects such as accretion of new subhalos and tidal truncation and disruption of old subhalos, these models

yield subhalo populations whose spatial distributions and mass functions agree well with results from N -body simulations (e.g., Taylor & Babul 2001, 2004; Benson et al. 2002; Zentner & Bullock 2003; Koushiappas et al. 2004; Oguri & Lee 2004; van den Bosch et al. 2005; Zentner et al. 2005). Our follow-up calculations will offer greater insight into the subtleties of time delay perturbations in a broader range of realistic circumstances, and better guidance as to how well we need to measure time delays if we want to probe dark matter substructure.

We have noted that in extraordinary lenses with close triplets of images in a cusp configuration, it may be possible to detect the effects of substructure through unambiguous changes in the arrival-time ordering of the images (compared to expectations for standard macromodels). We expect, though, that the real power of time delay millilensing will lie in its application to large ensembles of lenses with measured time delays. At present, time delay uncertainties are typically at the level of 1 day (see Oguri 2007 for a compilation). Improvements of a factor of a few are desired: our preliminary estimates indicate that improving the uncertainties to $\sim 0.5\%$ would yield constraints on substructure at the level of 0.3–0.5 dex in a given 4-image lens. Colley et al. (2003) have shown that coordinated global optical monitoring can yield time delays with uncertainties of less than 0.1 day. Monitoring at X-ray wavelengths, where variability can be rapid and dramatic, can yield even more precise time delays: Chartas et al. (2004) measure a time delay of 3.58 ± 0.14 hours between the two close images in PG 1115+080 with *Chandra* and *XMM-Newton* observations. With some effort, such techniques can probably be extended to a modest sample of time delays in the near future. Over the longer term, the advent of large time-domain surveys is expected to yield thousands of lensed quasars with time delays (e.g., Fassnacht et al. 2004; Kuhlen et al. 2004; Marshall et al. 2005; Kochanek et al. 2006). Even better would be a dedicated space platform capable of precise monitoring of lenses over extended periods of time (see Moustakas et al. 2008). Looking to the future, measuring precise image positions, flux ratios, and time delays in a sample of ~ 100 quad lenses could yield substructure measurements at the 20%–30% level or better. Since the measurements will span the redshift range $0.2 \lesssim z \lesssim 1$, this will provide a unique opportunity to study not just the amount of dark matter substructure but its evolution as well.

We thank Michael Kuhlen, George Meylan, Arlie Petters, and Eduardo Rozo for helpful conversations. We thank Masamune Oguri and the referee Neal Dalal for raising the issue of modeling uncertainties associated with multipole terms. CRK thanks Jonathan Faiwizewski for suggesting that the Central Limit Theorem might be helpful. CRK is supported by grant HST-AR-10668 from the Space Telescope Science Institute, which is operated by the Association of Universities for Research in Astronomy, Inc., under NASA contract NAS5-26555; and by NSF grant AST-0747311. The work of LAM was carried out at Jet Propulsion Laboratory, California Institute of Technology, under a contract with NASA.

APPENDIX
STATISTICS OF TIME DELAY PERTURBATIONS

In this Appendix we present an initial theory of the statistics of time delay perturbations. This theory rests on three assumptions: (1) subhalos are statistically independent (of each other; the probability of having a subhalo may still depend on position); (2) subhalos may be treated as point masses; and (3) time delay perturbations are dominated by changes in the lens potential (as opposed to changes in the image positions). The first assumption means that all subhalo positions and masses are drawn from the same probability distribution. This simplifies the theory, and seems reasonable for lensing since we work in projection and subhalos that are near each other on the sky are most likely well separated in space. The second and third assumptions will be relaxed in future work, but are adequate for our present goal of understanding in a general way how the time delay scatter depends on the amount of substructure and the subhalo mass function.

The lens time delay has the form given by Equation (1). By assumption #3, if we want to understand how substructure affects $\Delta t_{12} = \tau(x_1) - \tau(x_2)$, it is sufficient to study the potential difference $\Delta\phi_{12} = \phi(x_1) - \phi(x_2)$. Any change in the time delay is simply given by the change in the potential difference, multiplied by the time scale t_0 .

The potential due to a collection of N subhalos is the sum of contributions from individual subhalos. If the subhalos are point masses, the potential difference has the form

$$\Delta\phi_{12} = \sum_{i=1}^N \varphi(r_i, m_i), \quad \text{where} \quad \varphi(r, m) = \frac{\hat{m}}{\pi} \ln \frac{|x_1 - r|}{|x_2 - r|}. \quad (\text{A1})$$

If we can show that the mean and variance of φ are finite, then we can use the Central Limit Theorem to infer that the sum $\Delta\phi_{12}$ will be approximately Gaussian, and to determine the variance of $\Delta\phi_{12}$.

In order to compute the mean and variance of φ , we need to average over a subhalo's position and mass. Let $p_r(r)$ be the probability distribution for the subhalo's position, while $p_m(m) = (1/N)dN/dm$ is the probability distribution for its mass. Then the average of any function f has the form

$$\langle f \rangle \equiv \int dm p_m(m) \int dr p_r(r) f. \quad (\text{A2})$$

It is useful to note that smoothed substructure density distribution, $\kappa_s(r)$, may be written in terms of the position probability distribution:

$$\kappa_s(r) \equiv \int dm \frac{dN}{dm} \pi R_{\text{Ein}}^2 p_r(r) = \int dm \frac{dN}{dm} \hat{m} p_r(r) = N \langle \hat{m} \rangle p_r(r). \quad (\text{A3})$$

Now in order to determine the mean and variance of φ , we need to compute the moments

$$\begin{aligned} \langle \varphi \rangle &\equiv \int dm p_m(m) \int dr p_r(r) \frac{\hat{m}}{\pi} \ln \frac{|x_1 - r|}{|x_2 - r|} \\ &= \frac{1}{N\pi} \int dr \kappa_s(r) \ln \frac{|x_1 - r|}{|x_2 - r|}, \end{aligned} \quad (\text{A4})$$

$$\begin{aligned} \langle \varphi^2 \rangle &\equiv \int dm p_m(m) \int dr p_r(r) \frac{\hat{m}^2}{\pi^2} \left(\ln \frac{|x_1 - r|}{|x_2 - r|} \right)^2 \\ &= \frac{1}{N\pi^2} \frac{\langle \hat{m}^2 \rangle}{\langle \hat{m} \rangle} \int dr \kappa_s(r) \left(\ln \frac{|x_1 - r|}{|x_2 - r|} \right)^2. \end{aligned} \quad (\text{A5})$$

In both cases we used Equation (A3) to substitute for $p_r(r)$ in terms of κ_s . We also identified the mass integrals as yielding the averages $\langle \hat{m} \rangle$ and $\langle \hat{m}^2 \rangle$. The variance is then

$$\sigma_\varphi^2 = \langle \varphi^2 \rangle - \langle \varphi \rangle^2 \approx \langle \varphi^2 \rangle \approx \frac{1}{N\pi^2} \frac{\langle \hat{m}^2 \rangle}{\langle \hat{m} \rangle} \int dr \kappa_s(r) \left(\ln \frac{|x_1 - r|}{|x_2 - r|} \right)^2. \quad (\text{A6})$$

At the second step, we note that $\langle \varphi^2 \rangle \sim 1/N$ while $\langle \varphi \rangle^2 \sim 1/N^2$, so when there are many subhalos we may neglect the second term.

The integrands in Equations (A4) and (A5) diverge near x_1 and x_2 , but only logarithmically, and such a divergence is still integrable. As a result, as long as $\kappa_s(r)$ does not diverge badly near the image positions, the integrals are well behaved, so the mean and variance of φ are finite. This means the Central Limit Theorem holds, and we can infer that the potential difference $\Delta\phi_{12}$, and hence the time delay Δt_{12} , will have a distribution that is approximately Gaussian. (This argument also applies to clumps that are not point masses, because then any divergence in φ will be softer than logarithmic.)

Furthermore, thanks to the Central Limit Theorem we may compute the variance in $\Delta\phi_{12}$ as the quadrature sum of the variances of all the individual φ terms—or, in this case, a simple multiplication by N :

$$\sigma_\phi^2 \approx N \sigma_\varphi^2 \approx \frac{1}{\pi^2} \frac{\langle \hat{m}^2 \rangle}{\langle \hat{m} \rangle} \int dr \kappa_s(r) \left(\ln \frac{|x_1 - r|}{|x_2 - r|} \right)^2. \quad (\text{A7})$$

And of course $\sigma_t = t_0 \sigma_\phi$. Heuristically, we may summarize this result as

$$\sigma_t \propto \left(\kappa_s \frac{\langle m^2 \rangle}{\langle m \rangle} \right)^{1/2}, \quad (\text{A8})$$

where κ_s is indicative of the amount of substructure. While this expression oversimplifies the dependence on the spatial distribution of subhalos, it is conceptually instructive. In our simulations, we write $\kappa_s(r) = f_s \kappa_{\text{tot}}(r)$, and we keep the total mass distribution κ_{tot} fixed while we change the substructure mass fraction f_s . Therefore it is formally correct to write

$$\sigma_t \propto \left(f_s \frac{\langle m^2 \rangle}{\langle m \rangle} \right)^{1/2}. \quad (\text{A9})$$

This is our general conclusion for how the time delay scatter depends on the amount of substructure and the subhalo mass function. Note that if all subhalos have the same mass m , this simplifies to

$$\sigma_t \propto (f_s m)^{1/2}. \quad (\text{A10})$$

It is instructive to consider whether the Central Limit Theorem can be applied to flux ratios as well as time delays. For point mass clumps, the magnification of an image at position x has the form

$$\mu = [(1 - \phi_{xx})(1 - \phi_{yy}) - \phi_{xy}^2]^{-1}, \quad (\text{A11})$$

where

$$\phi_{xx} = - \sum_{i=1}^N \frac{\hat{m}}{\pi} \frac{(x-x_i)^2 - (y-y_i)^2}{|x-x_i|^4}, \quad (\text{A12})$$

and there are similar expressions for ϕ_{yy} and ϕ_{xy} . Now when we try to compute the mean and variance of each term by integrating over x_i , the integrand diverges non-integrably near x , and so the mean and variance diverge (also see Witt et al. 1995). The Central Limit Theorem therefore does not apply. The magnification probability distribution $p(\mu)$ may still be perfectly well defined, but it need not be Gaussian. Indeed, $p(\mu)$ can be computed analytically for a uniform distribution of point masses, and it is distinctly non-Gaussian (see §11.2 of Schneider, Ehlers & Falco 1992). There may be circumstances (say, certain types of spatially extended clumps) for which the Central Limit Theorem does apply to magnifications, but the theorem is not universally applicable as it is for time delays.

Returning to time delays, there is one last bit of theory that is useful. We intuitively expect that clumps far from the images have little effect on the time delay, but we can quantify this statement. Consider for simplicity images at $x_1 = (d, 0)$ and $x_2 = (-d, 0)$, and let us examine only subhalos at radii $r > R_0 \gg d$. We return to Equation (A7), plug in for x_1 and x_2 , and then take a Taylor series expansion to lowest order in d/r :

$$\epsilon_\phi^2 \approx \frac{1}{\pi^2} \frac{\langle \hat{m}^2 \rangle}{\langle \hat{m} \rangle} \int_0^{2\pi} d\theta \int_{R_0}^{\infty} dr r \kappa_s(r) 4d^2 \frac{\cos^2 \theta}{r^2} \approx \frac{4d^2}{\pi} \frac{\langle \hat{m}^2 \rangle}{\langle \hat{m} \rangle} \int_{R_0}^{\infty} \frac{\kappa_s(r)}{r} dr. \quad (\text{A13})$$

Notice that we have changed notation and written ϵ_ϕ to highlight that this is an error term—specifically, the rms error we make by neglecting subhalos beyond R_0 . We have computed the error in the potential, but we can relate it to the rms error in the time delay via $\epsilon_t = t_0 \epsilon_\phi$. (We have verified Equation (A13) using direct simulations of subhalo populations extending to large radii.) We have assumed for simplicity that the substructure mass distribution is circularly symmetric, $\kappa_s(r) = \kappa_s(r)$, but the generalization to elliptical symmetry is straightforward. For any reasonable substructure distribution, $\kappa_s(r)$ decreases as $r \rightarrow \infty$, so the integral converges. Not only that, but ϵ_t is a monotonically decreasing function of R_0 . In other words, the farther the subhalos are from the images, the less effect they have on the time delays. If we can tolerate some small error in time delays, we may neglect all subhalos beyond some threshold radius R_0 . Once we specify the time delay error tolerance, we can solve Equation (A13) to compute the threshold radius R_0 .

REFERENCES

- Amara, A., Metcalf, R. B., Cox, T. J., & Ostriker, J. P., 2006, *MNRAS*, 367, 1367
- Barnes, J., & Hut, P., 1986, *Nature*, 324, 446
- Bender, R., Surma, P., Döbereiner, S., Möllenhoff, C., Madejski, R. 1989, *A&A*, 217, 35
- Benson, A. J., Lacey, C. G., Baugh, C. M., Cole, S., & Frenk, C. S., 2002, *MNRAS*, 333, 156
- Blackburne, J. A., Pooley, D., & Rappaport, S., 2006, *ApJ*, 640, 569
- Bradač, M., Schneider, P., Lombardi, M., Steinmetz, M., Koopmans, L. V. E., & Navarro, J. F., 2004, *A&A*, 423, 797
- Bradač, M., Schneider, P., Steinmetz, M., Lombardi, M., King, L. J., & Porcas, R., 2002, *A&A*, 388, 373
- Browne, I. W. A., et al., 2003, *MNRAS*, 341, 13
- Blumenthal, J. S., Kravtsov, A. V., & Weinberg, D. H., 2000, *ApJ*, 539, 517
- Chartas, G., Dai, X., & Garmire, G. P., 2004, in *Carnegie Astrophys. Ser. 2, Measuring and Modeling the Universe*, ed. W. L. Freedman (Pasadena, CA: Carnegie Observatories); <http://www.ociw.edu/ociw/symposia/series/symposium2/proceedings.html>
- Chen, J., Kravtsov, A. V., & Keeton, C. R., 2003, *ApJ*, 592, 24
- Chen, J., Rozo, E., Dalal, N., & Taylor, J. E., 2007, *ApJ*, 659, 52
- Cheng, H.-C., Feng, J. L., & Matchev, K. T., 2002, *Phys. Rev. Lett.*, 89, 211301
- Chiba, M., 2002, *ApJ*, 565, 17
- Colín, P., Avila-Reese, V., & Valenzuela, O., 2000, *ApJ*, 542, 622
- Colley, W. N., et al., 2003, *ApJ*, 587, 71
- Congdon, A. B., & Keeton, C. R., 2005, *MNRAS*, 364, 1459
- Congdon, A. B., Keeton, C. R., & Osmer, S. J., 2007, *MNRAS*, 376, 263
- Dalal, N., & Kochanek, C. S., 2002, *ApJ*, 572, 25

- Davé, R., Spergel, D. N., Steinhardt, P. J., & Wandelt, B. D., 2001, *ApJ*, 547, 574
- Diemand, J., Kuhlen, M., & Madau, P. 2007, *ApJ*, 657, 262
- Dobler, G., & Keeton, C. R., 2006, *MNRAS*, 365, 1243
- Dodelson, S., & Widrow, L. M., 1994, *Phys. Rev. Lett.*, 72, 17
- Evans, N. W., & Witt, H. J., 2003, *MNRAS*, 345, 1351
- Falco, E. E., Gorenstein, M. V., & Shapiro, I. I., 1985, *ApJ*, 289, L1
- Fassnacht, C. D., Marshall, P. J., Baltz, A. E., Blandford, R. D., Schechter, P. L., & Tyson, J. A., 2004, *BASS*, 36, 1531
- Feng, J. L., 2005, *Ann. Phys.*, 315, 2
- Gao, L., White, S. D. M., Jenkins, A., Stoehr, F., & Springel, V., 2004, *MNRAS*, 355, 819
- Ghigna, S., Moore, F., Governato, F., Lake, G., Quinn, T., & Stadel, J., 2000, *ApJ*, 544, 616
- Helmi, A., White, S. D. M., & Springel, V., 2002, *Phys. Rev. D*, 666, 6, 063502
- Heyl, J. S., Hernquist, L., & Spergel, D. N. 1994, *ApJ*, 427, 165
- Jesseit, R., Naab, T., & Burkert, A., 2005, *MNRAS*, 360, 1185
- Kundić, T., Cohen, J. G., Blandford, R. D., & Lubin, L. M., 1997, *AJ*, 114, 507
- Keeton, C. R., 2001, *astro-ph/0102340*; <http://redfive.rutgers.edu/~keeton/gravlens>
- Keeton, C. R., 2003, *ApJ*, 584, 664
- Keeton, C. R., Burles, S., Schechter, P. L., & Wambsganss, J., 2006, *ApJ*, 639, 1
- Keeton, C. R., Gaudi, B. S., & Petters, A. O., 2003, *ApJ*, 598, 138
- Keeton, C. R., Gaudi, B. S., & Petters, A. O., 2005, *ApJ*, 635, 35
- Keeton, C. R., & Kochanek, C. S., 1997, *ApJ*, 487, 42
- Keeton, C. R., & Zabludoff, A. I., 2004, *ApJ*, 612, 660
- Klypin, A., Kravtsov, A. V., Valenzuela, O., & Prada, F., 1999, *ApJ*, 522, 82
- Kochanek, C. S., 2002, *ApJ*, 578, 25
- Kochanek, C. S., Dai, X., Morgan, C., Morgan, N., Poindexter, S., & Chartas, G., 2007, in *ASP Conf. Ser. 43, Statistical Challenges in Modern Astronomy IV*, ed. G. J. Babu & E. D. Feigelson (San Francisco, CA: ASP), 43; *arXiv:astro-ph/0609112*
- Kochanek, C. S., & Dalal, N., 2004, *ApJ*, 610, 69
- Kochanek, C. S., Mochejska, B., Morgan, N. D., & Stanek, K. Z., 2006, *ApJ*, 637, L73
- Kochanek, C. S., Schneider, P., & Wambsganss, J., 2004, Part 2 of *Gravitational Lensing: Strong, Weak & Micro, Proceedings of the 33rd Saas-Fee Advanced Course*, ed. G. Meylan, P. Jetzer, & P. North (Berlin: Springer-Verlag); *arXiv:astro-ph/0407232*
- Koopmans, L. V. E., Browne, I. W. A., & Jackson, N. J., 2004, *New Astron. Rev.*, 48, 1085
- Koopmans, L. V. E., & de Bruyn, A. G., 2000, *A&A*, 358, 793
- Koposov, S., et al., 2008, *ApJ*, 686, 279
- Koposov, S. E., Yoo, J., Rix, H.-W., Weinberg, D. H., Macciò, A. V., & Miralda-Escudé, J., 2009, *ApJ*, 696, 2179
- Koushiappas, S. M., Zentner, A. R., & Walker, T. P., 2004, *Phys. Rev. D*, 69, 043501
- Kravtsov, A. V., Gnedin, O. Y., & Klypin, A. A., 2004, *ApJ*, 609, 482
- Kuhlen, M., Keeton, C. R., & Madau, P., 2004, *ApJ*, 601, 104
- Lieu, R., 2008, *ApJ*, 674, 75
- Macciò, A. V., Kang, X., Fontanot, F., Somerville, R. S., Koposov, S., & Monaco, P. 2009, *arXiv:0903.4681*
- Macciò, A. V., Moore, B., Stadel, J., & Diemand, J., 2006, *MNRAS*, 366, 1529
- Mao, S., & Schneider, P., 1998, *MNRAS*, 295, 587
- Marshall, P., Blandford, R., & Sako, M., 2005, *New Astron. Rev.*, 49, 387
- Metcalf, R. B., 2005a, *ApJ*, 622, 72
- Metcalf, R. B., 2005b, *ApJ*, 629, 673
- Metcalf, R. B., & Madau, P., 2001, *ApJ*, 563, 9
- Metcalf, R. B., Moustakas, L. A., Bunker, A. J., & Parry, I. R., 2004, *ApJ*, 607, 43
- Metcalf, R. B., & Zhao, H., 2002 *ApJ*, 567, L5
- Momcheva, I., Williams, K., Keeton, C., & Zabludoff, A., 2006, *ApJ*, 641, 169
- Moore, B., Ghigna, S., Governato, F., Lake, G., Quinn, T., Stadel, J., & Tozzi, P., 1999, *ApJ*, 524, L19
- Morgan, N. D., Kochanek, C. S., Falco, E. E., & Dai, X., 2006, *arXiv:astro-ph/0605321*
- Moustakas, L. A., et al. 2008, in *Proc. SPIE 7010, Space Telescopes and Instrumentation 2008: Optical, Infrared, and Millimeter*, ed. J. M. Oschmann, M. W. M. de Graauw & H. A. MacEwen; *arXiv:0806.1884*
- Naab, T., & Burkert, A., 2003, *ApJ*, 597, 893
- Naab, T., Jesseit, R., & Burkert, A., 2006, *MNRAS*, 372, 839
- Oguri, M., 2007, *ApJ*, 660, 1
- Oguri, M., & Lee, J., 2004, *MNRAS*, 355, 120
- Pooley, D., Blackburne, J. A., Rappaport, S., & Schechter, P. L., 2007, *ApJ*, 661, 19
- Rest, A., van den Bosch, F. C., Jaffe, W., Tran, H., Tsvetanov, Z., Ford, H. C., Davies, J., & Schafer, J. 2001, *AJ*, 121, 2431
- Rix, H.-W., et al., 2004, *ApJS*, 152, 163
- Saglia, R. P., Bender, R., & Dressler, A. 1993, *A&A*, 279, 75
- Saha, P., 2000, *AJ*, 120, 1654
- Saha, P., & Williams, L. L. R., 2003, *AJ*, 125, 2769
- Schechter, P. L., & Wambsganss, J., 2002, *ApJ*, 580, 685
- Schneider, P., Ehlers, J., & Falco, E. E., 1992, *Gravitational Lenses* (Berlin: Springer-Verlag)
- Shin, E. M., & Evans, N. W., 2008, *MNRAS*, 385, 2107
- Sluse, D., et al., 2003, *A&A*, 406, L43
- Somerville, R. S., 2002, *ApJ*, 572, L23
- Strigari, L. E., Bullock, J. S., Kaplinghat, M., Diemand, J., Kuhlen, M., & Madau, P., 2007a, *ApJ*, 669, 676
- Strigari, L. E., Kaplinghat, M., & Bullock, J. S., 2007b, *Phys. Rev. D*, 75, 061303
- Taylor, J. E., & Babul, A., 2001, *ApJ*, 559, 716
- Taylor, J. E., & Babul, A., 2004, *MNRAS*, 348, 811
- van den Bosch, F. C., Tormen, G., & Giocoli, C., 2005, *MNRAS*, 359, 1029
- Weymann, R. J., et al., 1980, *Nature*, 285, 641
- Witt, H. J., Mao, S., & Schechter, P. L., 1995, *ApJ*, 443, 18
- Wyithe, J. S. B., Webster, R. L., Turner, E. L., & Mortlock, D. J., 2000, *MNRAS*, 315, 62
- Yoo, J., Kochanek, C. S., Falco, E. E., & McLeod, B. A., 2005, *ApJ*, 626, 51
- Yoo, J., Kochanek, C. S., Falco, E. E., & McLeod, B. A., 2006, *ApJ*, 642, 22
- Zentner, A. R., Berlind, A. A., Bullock, J. S., Kravtsov, A. V., & Wechsler, R. H., 2005, *ApJ*, 624, 505
- Zentner, A. R., & Bullock, J. S., 2003, *ApJ*, 598, 49